



Ni/SiO₂ catalysts for polyolefin deconstruction via the divergent hydrogenolysis mechanism

Brandon C. Vance^{a,b}, Pavel A. Kots^a, Cong Wang^a, Jack E. Granite^{a,b}, Dionisios G. Vlachos^{a,b,*}

^a Center for Plastics Innovation, University of Delaware, 221 Academy St., Newark, DE 19716, USA

^b Department of Chemical and Biomolecular Engineering, University of Delaware, 150 Academy St., Newark, DE 19716, USA

ARTICLE INFO

Keywords:

Plastics waste
Hydrogenolysis
Nickel
Earth-abundant metals
Circular economy

ABSTRACT

Noble metal-based hydrogenolysis is emerging as a key chemical deconstruction technology of polyolefins into valuable products. Still, the catalyst cost and availability are significant barriers to handling the large volume of plastics. Cheap earth-abundant metals have been deemed inactive for polyolefin hydrogenolysis. Herein, we report that Ni/SiO₂ is active in deconstructing low-density polyethylene to n-alkanes (C₆–C₃₅) at mild conditions (300 °C, 30 bar H₂) with maximum liquid yields of 65 wt%. We expose a new mechanism of long-alkane hydrogenolysis that encompasses chain location-dependent single and multiple C–C bond cracking events and rationalizes product selectivity and molecular weight dependence. Ni/SiO₂ catalysts are reusable and can handle multiple plastics producing feedstock-dependent products (i.e., n-alkanes, iso-alkanes, cyclics, aromatics, etc.). The findings broaden the scope of viable catalysts polyolefin hydrogenolysis and unleash the potential to manage the volume of plastic waste.

1. Introduction

The current linear (take, make, and waste) economy is harmful to natural environments. Plastics are mainly derived from fossil-fuels [1] with ~1 % from renewable bio-sources [2]. In the USA, 90 % of the plastics' carbon ends in landfills, incineration, or the environment [1,3,4], threatening the ecosystem [5–7] and human health [5,8,9]. The remaining is mechanically recycled, which degrades their physical properties [10]. Plastics waste chemical upcycling and deconstruction technologies are urgently needed.

Polyolefins (POs), such as polyethylene (PE) and polypropylene (PP), and polystyrene (PS) comprise ~66 % of plastics production [1] and are difficult to deconstruct due to the C–C bond stability. Several methodologies, such as hydrogenolysis [11–22], hydrocracking [23–25], pyrolysis [26], acid cracking [27], alkane metathesis [28,29], and non-conventional plasma [30] or microwave-assisted [31] chemistries, have been recently developed to deconstruct POs and PS to valuable lubricants, waxes, fuels and aromatics. Catalytic hydrogenolysis is particularly promising as it operates at mild temperatures (200–300 °C), requiring significantly lower energy than high-temperature pyrolysis and acid cracking, and has tunable product distributions. Noble metals (NMs), e.g., Ru, Pt, and Rh, have been predominately used and shown

tremendous potential. However, NMs are highly susceptible to heteroatom impurities (S, N, O, etc.) and contaminants of commercial plastic additives and waste streams [22], respectively. Their global reserves (~0.069 million metric tons (Mt) [32]) are tiny compared to the PO production (>215 Mt/yr[1]). Considering all NMs, a 1:10,000 catalyst-to-polymer ratio (far below the industrial minimum), and 0.1 wt % metal loading (all conservative estimates) reveals the scale of the problem: > 350 times the NM reserves are needed to handle the annual production scale of POs. Earth-abundant metals (EAMs), such as Ni, Co, Mo, etc., are 3–4 orders of magnitude cheaper [33], 10,000 times more abundant [34], and can handle impurities in hydrotreating petroleum feedstocks [35]. EAMs are active in small alkane hydrogenolysis [36–39] and plastics hydrocracking [40–43], but are ineffective for plastics hydrogenolysis [14–16]. Overcoming this scale barrier could advance the potential for commercialization.

Here, we demonstrate simple nickel on silica (Ni/SiO₂) catalysts to be comparably active to NMs for hydrogenolysis of low-density polyethylene (LDPE) with high yields of diesel and lubricant ranged hydrocarbons and low methane yields. They are regenerable and applicable even to commercial plastics. We introduce a mechanism incorporating single and multiple cracking events sensitive to the adsorbate location and alkane size, supported by stochastic simulations, and reconcile the

* Corresponding author at: Center for Plastics Innovation, University of Delaware, 221 Academy St., Newark, DE 19716, USA.

E-mail address: vlachos@udel.edu (D.G. Vlachos).

<https://doi.org/10.1016/j.apcatb.2022.122138>

Received 1 August 2022; Received in revised form 14 October 2022; Accepted 31 October 2022

Available online 2 November 2022

0926-3373/© 2022 Elsevier B.V. All rights reserved.

disparity with the small alkanes. We showcase the applicability of the catalyst to various everyday plastics, producing a slate of valuable products, and the promise of additional EAMs.

2. Methods

2.1. Catalyst synthesis

Nickel nitrate hexahydrate (Aldrich, $\text{Ni}(\text{NO}_3)_2 \cdot 6 \text{H}_2\text{O}$, $\geq 99.999\%$ trace metal basis) was used as received and silica-gel (Sigma-Aldrich, SiO_2 , Davisil grade 646, 35–60 mesh) was calcined in static air at 650°C for 3 h ($2^\circ\text{C}/\text{min}$ ramp) prior to synthesis. The xNi/SiO_2 catalysts, where x corresponds to the wt% Ni loading, were prepared by wetness impregnation of a nickel nitrate hexahydrate solution, dried in air at 110°C , and then calcined at 550°C for 3 h ($2^\circ\text{C}/\text{min}$ ramp).

2.2. Catalyst characterization

X-Ray diffraction (XRD) patterns were obtained on a Bruker D8 diffractometer with a 0.05° 2θ step size using $\text{Cu K}\alpha$ radiation (λ 1.54 Å). The average crystallite size was calculated using the Scherrer equation, $D = 0.90\lambda/(\beta\cos\theta)$, where θ is the diffraction angle and β is the full width at half-maximum.

N_2 sorption isotherms at -196°C were recorded on a Micromeritics ASAP 2020 instrument. Before measurements, the samples were degassed at 350°C for 3 h ($5^\circ\text{C}/\text{min}$ ramp).

Transmission electron microscopy (TEM) images were acquired on a Scanning/Transmission Electron Microscope, Talos F200C TEM/STEM. Samples were dispersed in ethanol and dropped on a lacey carbon TEM grid, then dried at room temperature for 15 min, then in the oven at 100°C for another 15 min.

N_2 dispersions were measured via N_2O titration [44] using the pulse technique on a Micromeritics AutoChem II connected to a Pfeiffer Vacuum Ominstar GSD 301 quadrupole mass spectrometer with secondary electron multiplier. Catalyst samples (150–200 mg) were reduced in-situ at 450°C for 1 h ($10^\circ\text{C}/\text{min}$) in 20 mL/min of a 10 % H_2/Ar flow. Samples were purged with He for 5 min and cooled to 50°C . Pure N_2O doses were delivered using a 0.5 mL sampling loop until complete saturation with 10 pulses. The mass spectrometer was calibrated using pure N_2 and N_2O pulses through the empty reactor. For quantification m/z 44 (N_2O) and m/z 28 (N_2) peaks were used. N_2 emission was used for dispersion calculations (Equation 7).

2.3. Hydrogenolysis reactions and product characterization

All polyethylene, polypropylene, and polystyrene samples from Aldrich were used directly without any preprocessing. Everyday polymer materials from SP Scienceware were cut into $\sim 1\text{ cm}^2$ pieces prior to reaction. Information of the polymer feedstocks is summarized in Table 1. Other chemicals and consumables used for product extraction and characterization are n-hexacosane ($\text{C}_{26}\text{H}_{54}$, Alfa Aesar, $\geq 99\%$), Raney-Nickel (Alfa-Aesar), methylene chloride (CH_2Cl_2 , HPLC grade, $\geq 99.9\%$), n-octacosane ($\text{C}_{28}\text{H}_{58}$, $\geq 98.0\%$), toluene- d_8 (Aldrich, 99 atom % D, 0.03 v/v% TMS), Whatman filter paper (GE, 11 μm).

Hydrogenolysis reactions were conducted in a 50 mL Parr stainless

steel batch reactor with a pressure gauge, thermocouple, and $25.4 \times 8\text{ mm}$ PTFE magnetic stir bar. A band heater connected to a PID controller was used to heat the reactor and maintain the reactor temperature.

Prior to reactions, the xNi/SiO_2 catalysts were reduced in 100 mL/min pure H_2 at 450°C for 2 h ($10^\circ\text{C}/\text{min}$ ramp). Before exposure to ambient conditions, the catalyst surface was passivated at 30°C for 15 min in 105 mL/min of a dilute air-He mixture (1 % O_2 concentration). 200 mg of the xNi/SiO_2 catalyst was added with 2.0 g of substrate to the Parr reactor for polymer reactions and only 50 mg of catalyst and 4.0 g of substrate were used for reactions with n-alkanes. All catalytic reactions were conducted solvent-free. The contents of the Parr reactor were well mixed using the stir bar. The Parr reactor was sealed and purged six times with H_2 at 15 bar before pressurizing to reaction pressure, typically 30 bar. The reactor was heated to reaction temperature, typically 300°C , and stirring was turned on at 500 rpm when the reactor temperature reached the substrate melting temperature (PE 140°C , PP 160°C , PS 240°C , $n\text{C}_{26}$ 56°C). Reactions were maintained for specified intervals (1 – 12 h) after the reaction reached reaction temperature and then quickly quenched in an ice bath. Products were collected once the reactor temperature fell below 2°C .

Gas samples from the Parr reactor headspace were charged in a 1 L Tedlar gas sampling bag and analyzed with GC-FID (Agilent CP-Volamine GC column). The residual solid-oil mixture was combined with $\sim 20\text{ mL}$ of methylene chloride containing 20 mg of n-octacosane as an internal standard. This mixture was separated by filtration. The liquids were quantified using a GC-FID (Agilent HP-1 column) and identified using a GC-MS (Agilent DB-1 column). Calibration coefficients and retention times for products were measured by injection of $\text{C}_1\text{--C}_{35}$ analytical standards (Figs. S1–S2).

For experiments with polymer, the solid residues collected after filtration were analyzed using differential scanning calorimetry (DSC) using a Discovery DSC (TA Instruments). Samples were sealed in aluminum containers and heated in a nitrogen flow from 30°C to 200°C ($10^\circ\text{C}/\text{min}$) and held at 200°C for 5 min.

2.4. NMR analysis

All solution ^{13}C NMR experiments were carried out with the 5-mm broadband probe (BBFO) on either a Bruker AVIII 600 MHz or a Bruker AVIII 400 MHz instrument. Spectra for the neat LDPE were collected at 100°C in tetrachloroethane- d_4 , whereas the solid residues were collected at 75°C in toluene- d_8 . The variable temperature ^{13}C experiments were conducted using a 5 mm BBFO probe on the 400 MHz instrument with the proton decoupling. The chemical shift was calibrated via the solvent peaks. A standard temperature calibration sample (80 % ethylene glycol in DMSO- d_6) was used to calibrate the probe temperature under the similar conditions as used for the variable temperature measurements.

2.5. GPC analysis

Samples of oil were dissolved in THF (1 mg/mL) and analyzed using GPC on a Waters e2695 instrument equipped with three Styragel columns connected in sequence: HR0.5, HR3 and HR4 with THF as the

Table 1
Polymer feedstocks used in hydrogenolysis reactions.

Feedstock Classification	Polymer	Chemical Formula	Vendor	Molecular Weight (kDa)	Tacticity	Referencing in Text
Virgin Granules	Low-density polyethylene	$[\text{CH}_2]_n$	Aldrich	~ 4	–	4LDPE
	Low-density polyethylene	$[\text{CH}_2]_n$	Aldrich	~ 76	–	76LDPE
	Polypropylene	$[\text{CH}_2\text{CH}(\text{CH}_3)\text{CH}_2]_n$	Aldrich	~ 12	Isotactic	12PP
	Polypropylene	$[\text{CH}_2\text{CH}(\text{CH}_3)\text{CH}_2]_n$	Aldrich	~ 250	Isotactic	250PP
	Polystyrene	$[\text{CH}_2\text{CH}(\text{C}_6\text{H}_5)]_n$	Aldrich	~ 35	–	PS
Everyday polymers	Polyethylene bottle (240 mL)	$[\text{CH}_2]_n$	SP Scienceware	–	–	PE bottle
	Polypropylene bottle cap (240 mL)	$[\text{CH}_2\text{CH}(\text{CH}_3)\text{CH}_2]_n$	SP Scienceware	–	–	PP cap

mobile phase at 0.3 mL/min flow rate. A refractive index detector was used and a standard PS calibration kit (WAT058931) was injected to calibrate the retention time.

2.6. Catalyst regeneration

Hexanes (Fisher Chemical, $\geq 98.5\%$), methylene chloride (CH_2Cl_2 , HPLC grade, $\geq 99.9\%$) were used as received. $15\text{Ni}/\text{SiO}_2$ was used for reusability experiments. Spent $15\text{Ni}/\text{SiO}_2$ was collected after 12 h of reaction to attain full deconstruction of solids. The spent catalyst was separated from liquid products via filtration described above and allowed to dry in air overnight. Then the spent catalyst was washed with 20 mL of hexanes followed by 20 mL of methylene chloride and dried in air overnight. Afterwards, the spent catalyst was reduced using the same procedure for the fresh catalyst, described above.

2.7. Stochastic modeling of nC26 hydrogenolysis

The divergent hydrogenolysis mechanism on C26 was modeled stochastically using the direct application of the Gillespie algorithm [45] with propensities estimated by the relative experimental rates. Possible events include: 1) C26 adsorption, 2) C26 desorption, 3) terminal cracking, 4) internal cracking, 5) desorption of products, 6) terminal cracking cascades on products, and 7) readsorption of products. The adsorption of C26 was assumed to be equilibrated, and the probability of adsorbing any C-C bond in the alkane chain was uniform.

For nC26, nC₂₅ is produced only via terminal cracking while C₁₃ is only produced via internal cracking at low conversions. Thus, the relative C-C cracking rates can be estimated from their experimental molar ratio. Based on our data, the terminal cracking is 25 times faster than interior cracking, in qualitative agreement with the Ni hydrogenolysis of small alkanes.[39].

The propensity of the terminal and internal cracking was set to 1 and 1/25, respectively. The propensity for nC26 desorption is 1 since the desorption and terminal cracking rates are comparable. Cracking produces two fragments that could undergo successive terminal cracking or

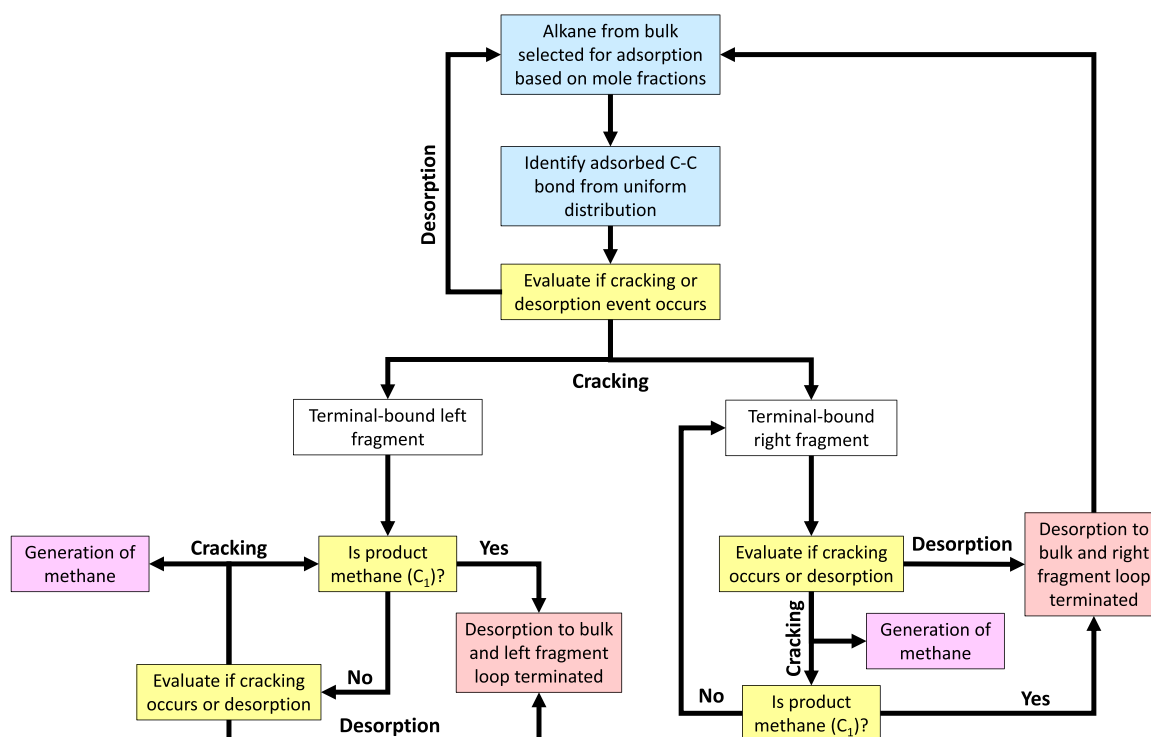
hydrogenate and desorb. n-Alkane desorption rates over Pt and graphite are inversely proportional to the carbon number [46,47]. We expect a similar trend on Ni. Thus the desorption propensity was modeled as a decaying exponential function $P = \exp[-0.5(26 - n)]$, equal to 1 when $n = 26$. When C₁ was produced, desorption was instantaneous. Once both fragments had desorbed, the population of alkyl chains in the bulk was updated and adsorption of a new molecule from the bulk was allowed. The adsorption propensity for each alkane was calculated as that alkane's respective concentration. The starting number of C26 molecules was 40,000. The number of stochastic events was varied to obtain differential (5–7 %) conversions. 500 runs were repeated for each condition for statistical certainty. Scheme 1 is a stepwise representation of the algorithm used to run these simulations. Identification and evaluation steps used random numbers to determine alkane selection, C-C bond adsorption, and event occurrence based on the propensities.

3. Results and discussion

3.1. Effect of nickel loading and reaction conditions on catalyst performance

The metal loading and dispersion strongly influence small alkane hydrogenolysis [48,49] and PO hydrogenolysis [13,21]. Fig. 1a shows a typical carbon distribution from 4LDPE (Sigma, $M_w \sim 4$ kDa) deconstruction at 300 °C for 2 h over $15\text{Ni}/\text{SiO}_2$ (the number in front of Ni indicates the wt%). Excitingly and in stark contrast to previous reports, moderate methane and a broad range of liquid products form, consisting chiefly of n-alkanes (liquid and gas) with $\lesssim 25\%$ of isomers, and a maximum at C₂₂.

The product yield (Fig. 1b and Fig. S3) is sensitive to the Ni loading (commercial Raney-Ni is taken as a surrogate of 100 wt% Ni) with a sharp optimum at 15 wt%, however the individual carbon product distributions are nearly identical, regardless of the Ni loading (Fig. 1a and Fig. S4). Differential scanning calorimetry (DSC) of the solid residues exposes macromolecule transformations when the polymers come in contact with the catalyst [19,20,23,24]. Low activity catalysts give DSC



Scheme 1. Algorithm workflow used to simulate the divergent hydrogenolysis of n-hexacosane.

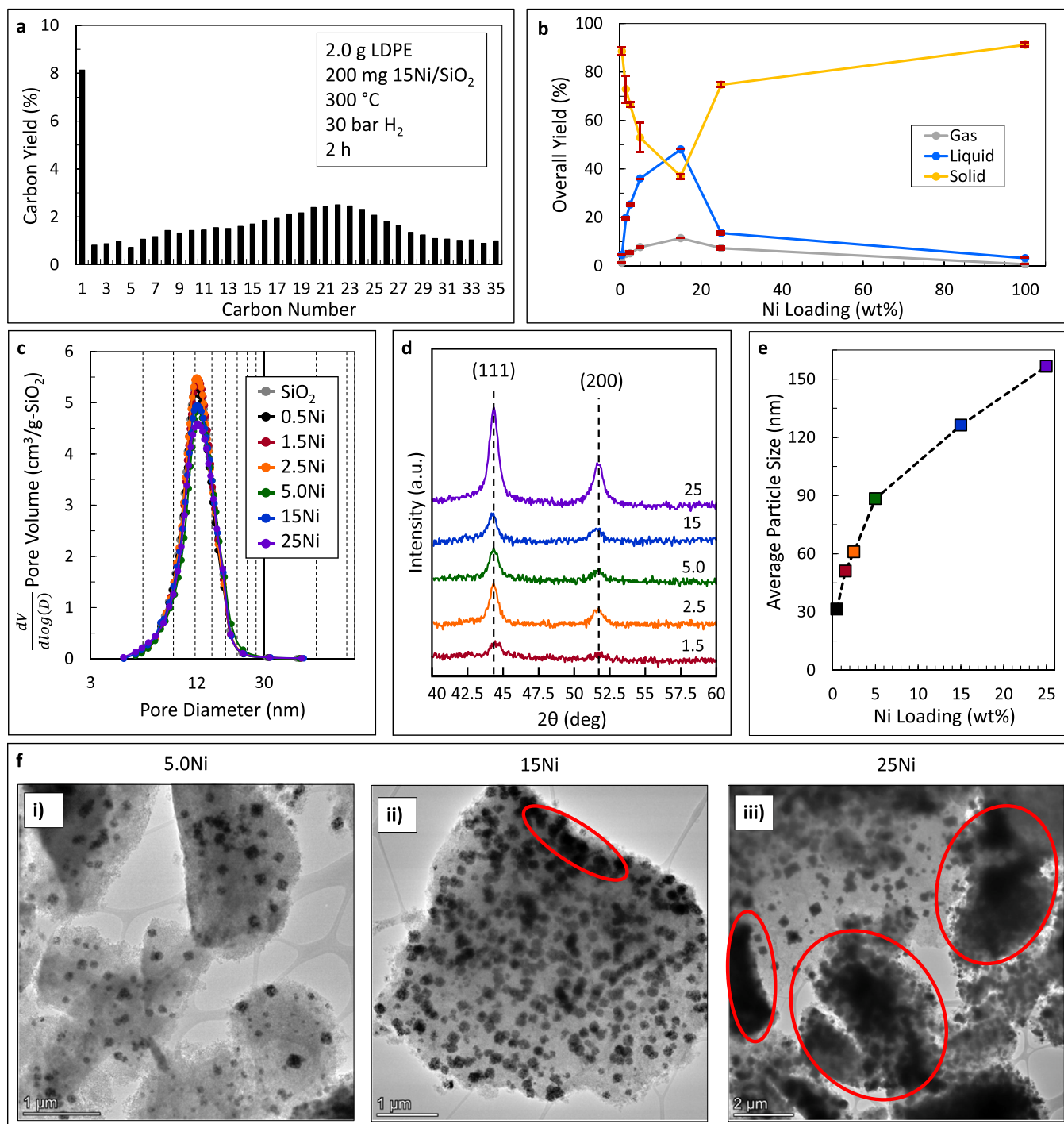


Fig. 1. Effect of Ni loading in Ni/SiO₂ catalysts and LDPE hydrogenolysis. a, Typical carbon product distribution over 15Ni/SiO₂. b, Overall product yields vs. Ni loading. c, BJH pore size distribution from N₂ sorption. d, XRD patterns of the Ni/SiO₂ catalysts. e, Average particle size vs. Ni loading. f, TEM micrographs of Ni particle agglomeration circled in red. i, 5Ni/SiO₂. ii, 15Ni/SiO₂. iii, 25Ni/SiO₂. Reaction conditions: 2.0 g 4LDPE (*M_w* ~4 kDa), 200 mg xNi/SiO₂, 300 °C and 30 bar H₂ for 2 h.

peaks similar to the neat polymer, indicating minimal solid reactions (Fig. S5). Conversely, the 15Ni/SiO₂ DSC is broad and peaked at much lower temperatures, manifesting a significant polymer size reduction from 4 to ca. 0.3–0.7 kDa. 1.5–5Ni/SiO₂ catalysts reduce the chain size less, with a feature at 85 °C (*M_w* ~0.5 kDa).

N₂ sorption indicates Ni does not impact the SiO₂ surface area or mesoporosity (Fig. 1c and Fig. S6). XRD of the reduced catalysts (Fig. 1d) shows Ni(111) and Ni(200) facets and a broad 16–28° peak due to the amorphous silica. The ratio of the Ni facets is constant (ca. 2.5) over the

studied loading range and crystallite sizes (Table S1). TEM shows large cubic particles (>20 nm) with a log-normal size distribution (Figs. S7–S9). The particle size distribution broadens with increasing Ni loading from 31 to 157 nm (Fig. 1e). The overall size and shape of the Ni particles are maintained before and after reduction, but the large cubic particles exhibit a spongy microstructure, and consist of several interconnected ca. 10–15 nm crystallites (Fig. S10), typical for Ni/SiO₂ [50]. TEM of the 0.5–5.0Ni/SiO₂ shows homogeneously dispersed particles on the SiO₂ support. Agglomeration occurs for higher loadings (circled in

red in Fig. 1f.i-ii), manifested as large dark spots ($\geq 1 \mu\text{m}$) in the micrographs. 15Ni/SiO₂ shows mild agglomeration with sparse dark spots, whereas 25Ni/SiO₂ demonstrates extensive agglomeration (Fig. 1f and Fig. S11). Catalyst productivity normalized to the quantity of exposed Ni atoms, measured using N₂O titration [44], displays an optimum at 5.0 wt% (Table 2) and sharply decreases for higher loadings due to particle agglomeration. Characterization data shows that particle agglomeration leads to decline in active site density leading to reduced productivity at high loadings. Below, we focus on the 15Ni/SiO₂ catalyst as it has the highest apparent productivity.

The reaction temperature and H₂ pressure strongly influence the PO hydrogenolysis activity over Ru- and Pt-based catalysts [12,15–17,20]. The activity is marginal at 285 °C but high at ≥ 300 °C, consistent with the DSC data (Figs. S12–S13). At 315 °C, the product yields and selectivities are comparable (Figs. S14–S15), but the molecular weight distribution of the solids are narrower (sharper DSC features) due to increased rates of C–C bond cleavage on the polymer backbone.

The activity shows a sharp maximum with respect to H₂ partial pressure with a 3x lower solid yield at 30 bar than at 20 and 40 bar (Figs. S16–S17). Similar activity trends have been reported in PO hydrogenolysis over Ru-based catalysts [13,22]. This activity trend is associated with the competition between H₂ and alkane (or polyethylene) for binding sites [13,51]. Relatively low hydrogenolysis rates occur at low and high H₂ pressures due to the metal surface being saturated by alkane or hydrogen, respectively. Optimal hydrogenolysis rates are observed when the hydrogen and alkyl surface concentrations are balanced. Interestingly, the optimal H₂ pressure for Ru-based catalysts spans the range of 30–45 bar, comparable to Ni/SiO₂ but the optimum is much less sharp. This indicates the reactivity trend and optimal H₂ pressures are metal-sensitive. Taken together, optimizing the temperature, pressure, and catalyst loading rationalizes why previous studies [15,16] deduced Ni catalysts as inactive.

3.1.1. Comparative catalyst performance and slate of LDPE-derived products

The solids undergo significant deconstruction at early times, forming 47 % liquids in 2 h (Fig. 2a), and their DSC peaks significantly shift from 104 °C for neat 4LDPE to 90 and 60 °C at 1 and 2 h, respectively ($M_w \sim 0.4$ kDa) (Fig. 2b). This transition in the melting points demonstrates a progressive reduction in the molecular weight of 4LDPE and the solid residues. Longer reaction times (2–4 h) do not provoke changes in the solids (similar DSC peaks), but the solid molecular weight distribution becomes sharper, making only an additional 10 % of liquid (~ 57 % total). The sharpening is intense at 6 h with a peak at 65 °C and a shoulder at 55 °C. The invariant liquid and gas yields (3–6 h) arise from the catalytic sites being preoccupied with solid transformations. Upon solid deconstruction at 9 h, 65 % of liquids form.

¹³C NMR of the neat 4LDPE shows a dominant resonance at 29.0 ppm, corresponding to CH₂ groups in the chain backbone [52]. CH₃ end group resonances appear at 13.3 ppm accompanied by less intense resonances of CH₂ groups in the beta (22.0 and 22.4 ppm) and gamma

positions (31.2 ppm). Weak resonances at 37.1 ppm and 33.5 ppm, associated to methine carbons and CH₂ groups adjacent to the methine carbon, respectively, indicate the neat 4LDPE has ~ 1.5 short-chain branches per 100 CH₂ groups.

The solid residues were also characterized using ¹³C NMR with different solvent and temperature (see Methods), resulting in a down-field shift of all peaks. Fig. 2g shows that the spectra of the solid residues are similar to the initial 4LDPE with a major peak at 29.7 ppm and a small shoulder at 29.3 ppm due to CH₂ groups in the backbone. Less intense resonances of CH₃ end groups appear at 13.7 ppm along with the associated CH₂ groups in the beta (22.6 ppm) and gamma positions (31.9 ppm) to the CH₃ group. Chain branching is absent, as evident by the lack of methine carbons (~ 38 ppm), CH₂ groups next to methine carbons (35 ppm), and CH₃ groups, typical for short chains (11 ppm). Thus, the solid residue at all reaction times is a mixture of normal alkanes. This is consistent with GCMS data, that shows a lack of tertiary carbons in the liquid products. The disappearance of tertiary carbons in the solid residues compared to initial LDPE suggests that short-chain branching points may serve as initiation locations for hydrogenolysis, as they react in the first hour of the reaction. We estimate the average carbon number of solids from the peak areas of CH₂ and CH₃ groups (Fig. 2c and Fig. S19). The dominant melting temperature peak in the DSC curves (Fig. 2b) was used to estimate the carbon number by cross-referencing the maximum on the melting curve with the known melting temperature for pure n-alkanes. Unexpectedly, the carbon number grows from 2 to 4 h and then sharply drops at 6 h, congruent with the DSC data (Fig. 2b). This highlights a complex reaction system on the residual polymer encompassing solid-solid transformation involving C–C bond scission and formation and/or a preferential deconstruction of alkyl chains in the C₃₀–C₄₀ range. Previous reports [53] show the possibility of C–C bond formation in conjunction with hydrogenolysis due to microreversibility.

Importantly, the liquid products comprise valuable diesel (C₉–C₂₂) and lubricant base oils (C₂₀₊) (Fig. 2d). The methane selectivity is surprisingly low (17 % at 9 h), despite Ni's demethylation selectivity (>50 %) for small alkanes [36,54]. The C₁–C₃₅ selectivities are stable between 1 and 6 h due to no secondary reactions (Fig. 2d and Fig. S20). The data suggests strong competitive adsorption between the residual polymer and the products, consistent with hydrocracking[24] and hydrogenolysis [12,21] over other catalysts. Upon solids consumption, the larger products transform into lighter alkanes. The selectivity (Fig. 2e) to "lights" (C₂–C₁₉) grows continually with a secondary generation at 95–100 % solid deconstruction. Conversely, the yield of "heavies" (C₂₀–C₃₅) reduces at 100 % deconstruction by secondary hydrogenolysis, resulting in a bell-shaped selectivity curve (Fig. 2f). The secondary consumption is more pronounced for the larger hydrocarbons.

The performance of Ni/SiO₂ is comparable to NM-based catalysts. Reaction temperatures are similar to Pt and ~ 50 °C higher than Ru, while reaction times are similar or shorter. The diesel carbon distribution and yield (40–70 %) are comparable to NM catalysts; the selectivity to methane is comparable to Ru (7–25 %) [15,20] and lower than Pt (25–40 %) [12]. The apparent productivity (Equation 5 in Supplementary Information) of 15Ni/SiO₂ is $2.40 \left(\frac{\text{g}_{\text{liquid}}}{\text{g}_{\text{cat}} \cdot \text{h}} \right)$ at 2 h and $0.73 \left(\frac{\text{g}_{\text{liquid}}}{\text{g}_{\text{cat}} \cdot \text{h}} \right)$ at 9 h and full deconstruction. Based on the recent analysis [55], Pt hydrogenolysis has apparent productivities in the range of 0.15–0.25 $\left(\frac{\text{g}_{\text{liquid}}}{\text{g}_{\text{cat}} \cdot \text{h}} \right)$ at full deconstruction, whereas Ru's full deconstruction apparent productivities span 0.54–12 $\left(\frac{\text{g}_{\text{liquid}}}{\text{g}_{\text{cat}} \cdot \text{h}} \right)$. 15Ni/SiO₂ is competitive with both metals but requires a ~ 50 °C higher processing temperature compared to Ru-based catalysts. Recently, we showed the overall cost-benefit analysis of plastic hydrogenolysis should consider both reaction time and temperature. Therefore, relatively short reaction times over 15Ni/SiO₂ will guarantee energy efficiency despite a higher operating temperature.

Table 2
Ni dispersion and productivities Ni/SiO₂ catalysts.

Catalyst	Ni Dispersion (%)	Apparent productivity $\left(\frac{\text{g}_{\text{liquid}}}{\text{g}_{\text{cat}} \cdot \text{h}} \right)$	Exposed Ni Productivity $\left(\frac{\text{g}_{\text{liquid}}}{\text{g}_{\text{Ni}} \cdot \text{h}} \right)$
0.5Ni/SiO ₂	23	0.23	200
1.5Ni/SiO ₂	–	0.99	–
2.5Ni/SiO ₂	3	1.3	1800
5.0Ni/SiO ₂	2	1.8	2300
15Ni/SiO ₂	2	2.4	690
25Ni/SiO ₂	2	0.68	140
Raney Ni	–	0.16	–

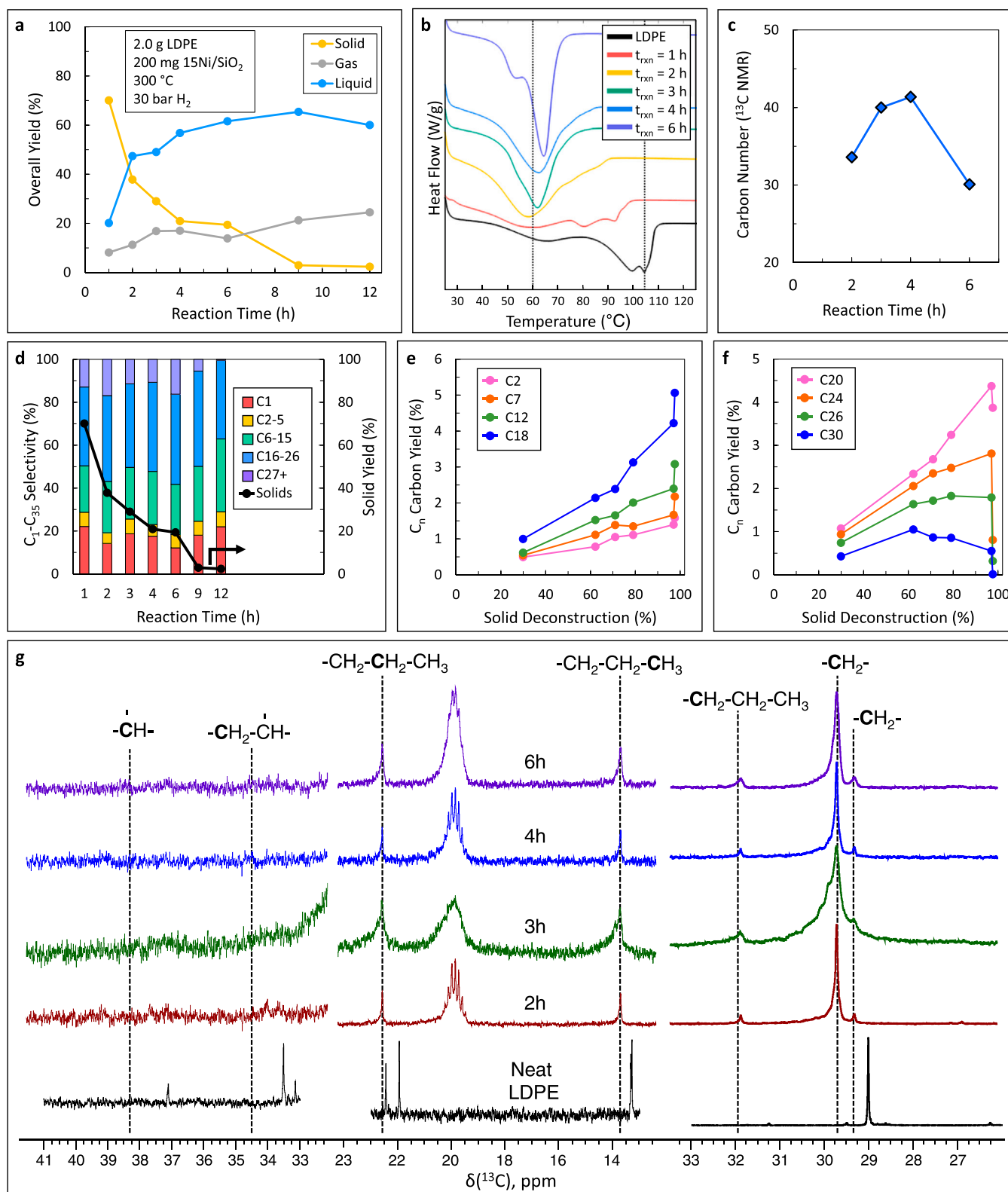


Fig. 2. Time-dependent LDPE hydrogenolysis over 15Ni/SiO₂. a, Overall product yields vs. reaction time. b, Time-dependent DSC curves from solid residues. c, Carbon number in the solids from the CH₂ and CH₃ peak areas in the NMR spectra. d, C₁-C₃₅ carbon selectivities vs. reaction time. e, f, Carbon yield for selected products. g, ¹³C NMR spectra of the time-dependent solid residues at 75 °C. Reaction conditions: 2.0 g 4LDPE (M_w ~4 kDa), 200 mg 15Ni/SiO₂, 300 °C and 30 bar H₂.

3.2. Catalyst reuse

The 15Ni/SiO₂ catalysts were tested for their reusability after reactions operating at full deconstruction of 4LDPE. Spent catalyst was collected by filtration and directly reused. The catalyst activity declines by ca. 5 % after each reuse (Fig. 3a), while the selectivity remains constant (Fig. 3b). Thermogravimetric analysis in air (Fig. 3c) indicates

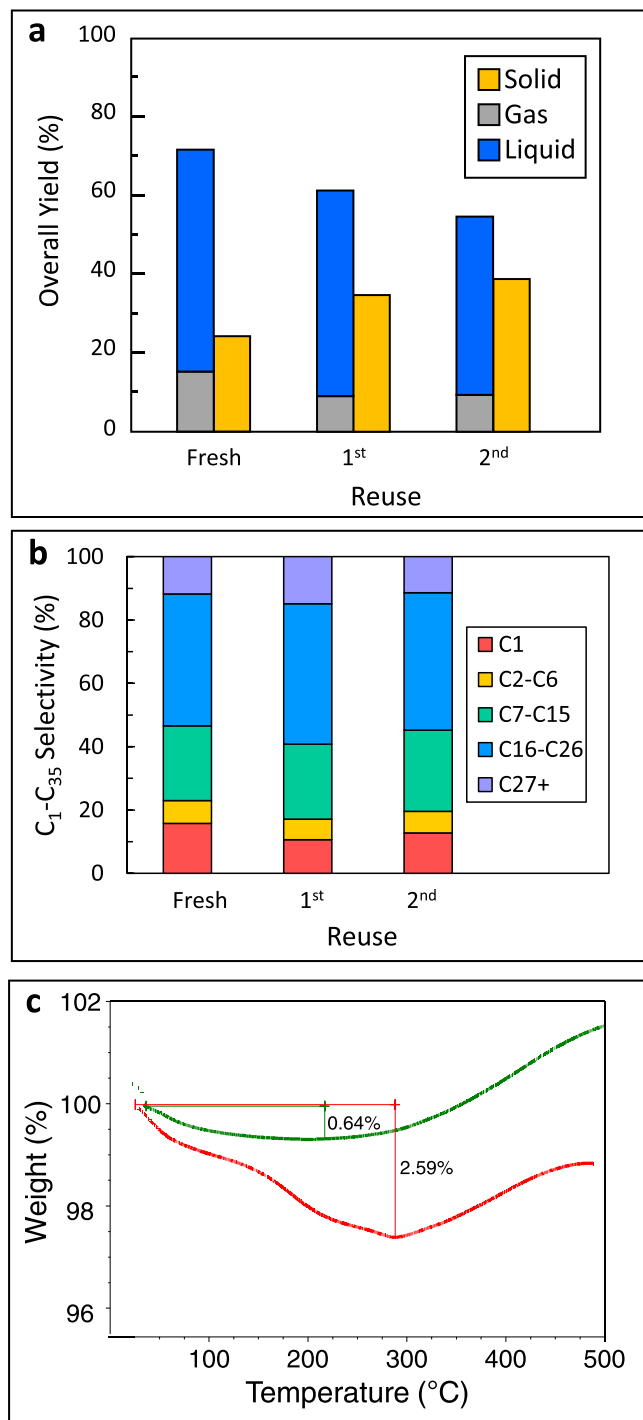


Fig. 3. Reuse of 15Ni/SiO₂ for the hydrogenolysis of LDPE. a, Overall yield of solids, liquid, and gas products for the fresh, single reuse, and double reused catalyst, (b) Carbon selectivities for C₁-C₃₅ products as a function of catalyst reuse, (c) TGA of the unused catalyst (green) and 15Ni/SiO₂ catalyst after one reuse (red). Reaction conditions: 2.0 g 4LDPE, 200 mg 15Ni/SiO₂, 300 °C, 30 bar H₂ for 2 h.

minor deposits of light carbonaceous species (~2 wt%) remain on the catalytic surface post-reaction, likely responsible for the reduced activity. These carbon deposits are likely chemisorbed alkyl chains or unrecovered higher alkanes rather than coke as they are removed completely above 300 °C to fully regenerate activity. The increase in weight loading above 300 °C is attributed to the oxidation of the bulk Ni nanoparticles as it is seen for both the fresh and spent catalysts. TEM of the catalyst after reaction (Figs. S21–S22) show the Ni nanoparticle size and structure are effectively identical to the fresh catalyst samples. The spent catalyst after two reuses has a dispersion of 27 % similar to the fresh catalyst (Table 2), indicating the Ni nanoparticles are resistant to sintering and further demonstrating their stability.

The performance, reusability, cost, and abundance highlight the immense promise of Ni catalysts for PO hydrogenolysis. Other EAMs are also active for PO hydrogenolysis (Fig. S23), underscoring the importance of this class of materials and broadening the viable catalytic metals for polyolefin hydrogenolysis.

3.3. Mechanistic insights

n-Hexacosane (nC26) hydrogenolysis experiments indicate that nC26 is significantly more active than 4LDPE—it requires an eightfold dilution (reactant-to-catalyst ratio) to limit the conversion to 5–30 % in 1–6 h at 300 °C. Unlike PO hydrogenolysis, where methane is a small fraction, methane and n-pentacosane (nC25) are the predominant products (Fig. 4a and Figs. S24–S25), showcasing C-C terminal cracking congruent with smaller alkanes [36,39,54]. The nonlinear molecular size distribution illustrates complex reaction pathways. We characterize this behavior by introducing $\chi_i = [C_i]/[C_{26-i}]$ (see Methods). A single cracking event should yield $\chi_i = 1$ for all i 's and $\chi_i \neq 1$ indicates successive reactions on oligomer i ($\chi_i < 1$) or 26- i ($\chi_i > 1$). χ_{12} is unity, χ_1 is 5.4 and all $\chi_2, \dots, \chi_{11} < 1$ (Fig. 4b). Single cracking occurs only near the very middle of the chain, and ~5–6 terminal cascades happen on nC26. χ_1 for nC20 (Fig. S25) is 1.9, demonstrating terminal cascades are less prevalent in shorter hydrocarbons.

We verify this proposed divergent hydrogenolysis mechanism comprised of single and multiple C-C scission events on the terminal and interior carbons, depicted in Fig. 5, via stochastic simulations using a straightforward application of the Gillespie algorithm (see Methods). Bigger chains stay longer on the catalyst due to their stronger, size-dependent adsorption [46,47]. We infer that terminal cracking is extremely fast and desorption is slow (see Methods). Longer chains may undergo a single terminal C-C cracking event (path R1; paths depicted in Fig. 5c), producing one methane and a smaller chain, but frequently experience multiple terminal C-C scissions to generate several methane molecules (path R2) until the fragment is sufficiently tiny to be weakly adsorbed and leave the surface (Fig. 5a). Adsorption at the chain interior is quasi-equilibrated with the bulk liquid because internal C-C bond cleavage is slow (path R3) (Fig. 5b). nC26 hydrogenolysis experiments using D₂ support this conjecture because all products have the same fraction of deuteration and no nC26 is obtained after reaction without undergoing H-D exchange (Fig. 4c and Figs. S26–S27). Internal cracking (path R3) is followed by hydrogenation and desorption or multiple terminal C-C scissions (path R4). The hydrogenolysis of small alkanes (C₂-C₁₀) over a variety of metals (i.e., Ru, Pt, Fe, Ni, etc.) [36,38,56] is usually described by a single pathway to capture the reaction outcome. The hydrogenolysis of nC26 differs from the behavior of small alkanes because four chemically-independent hydrogenolysis pathways are required to describe the reaction behavior.

Fig. 4d,e shows the predicted molecular and χ distributions, respectively. The model and experimental product distributions are qualitatively similar, with significant fractions of C₁ and C₂₅ products and a flat production of C₂-C₂₄ alkanes. The predicted χ_1 and $\{\chi_{10}, \chi_{11}, \chi_{12}\}$ values are close to the experimental results but lack fine details, which are attributed to the simplifying assumptions in the adsorption and kinetic phenomena of nC26 (see Methods). Coupling these

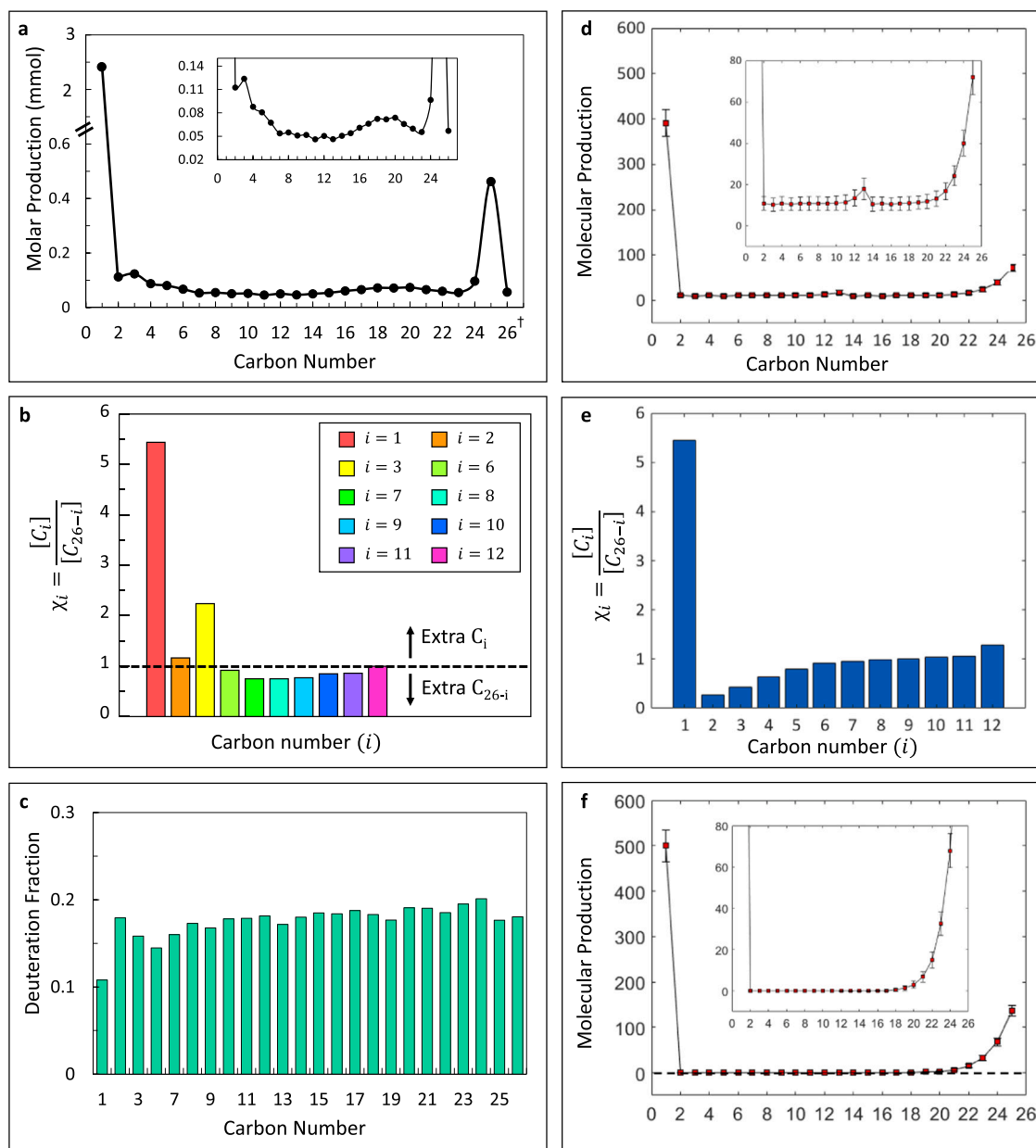


Fig. 4. Kinetic and stochastic modeling of n-hexacosane (nC26) hydrogenolysis over 15Ni/SiO₂ with conversion 5–30 %. a,b, Typical experimental molar C₁–C₂₆ product and χ distributions (see text). c, Fraction of H-atoms in nC26 and n-alkane products replaced by deuterons after deuterium hydrogenolysis. d,e, Prediction of C₁–C₂₅ molecular products and χ distributions. f, Same as d with only terminal cracking. Insets are zoomed-in views. Reaction conditions: 4.0 g nC26, 50 mg catalyst, 300 °C, 30 bar H₂ for 2 – 6 h. Experiments with D₂ used 30 bar D₂ for 4 h.

stochastic simulations with molecular dynamic and density functional theory calculations should provide the information needed to capture the fine-structure behavior in the experimental and χ_i distributions. Nonetheless, the model matches well with the nC20 hydrogenolysis data used for model validation (Fig. S25). Importantly, a single pathway (e.g., only R1, R2, or R3) cannot predict the experimental data (Fig. S28 and Fig. 4f). The simulations strongly support that the orchestration of all pathways in Fig. 5c drives hydrogenolysis and product selectivity.

Excitingly, the mechanism can rationalize the hydrogenolysis of LDPE and the impact of molecular weight. Ni catalysts favor intrinsically terminal over internal cracking. Terminal C–C bonds are approximately tenfold more abundant in nC26 than 4LDPE, explaining the higher reactivity of nC26 and the effect of molecular weight more generally. Ni is less likely to initiate LDPE terminal cracking by the R1 or R2 pathways despite its higher activity for terminal bond rupture; instead,

hydrogenolysis proceeds via internal scissions (R3 and R4 pathways) due to the interior bond abundance and higher probability of being on the surface. The carbon selectivities (Fig. S29 and Fig. 2d) at similar deconstructions show that 4LDPE generates approximately fourfold more methane than nC26 due to the R4 terminal cascade producing methane until the chain is small enough to leave the surface. nC20 is sufficiently small that all lighter hydrocarbons escape secondary reactions as evident from the selectivity (Fig. 2e, f) and χ_i data. Similar mechanistic insights could be drawn for other catalytic metals after adjusting the individual rates of the four reaction pathways.

3.4. Feedstock diversity

The catalyst is active on virgin granules of 4LDPE ($M_w \sim 4$ kDa), 76LDPE ($M_w \sim 76$ kDa), 12PP ($M_w \sim 12$ kDa), 250PP ($M_w \sim 250$ kDa), PS

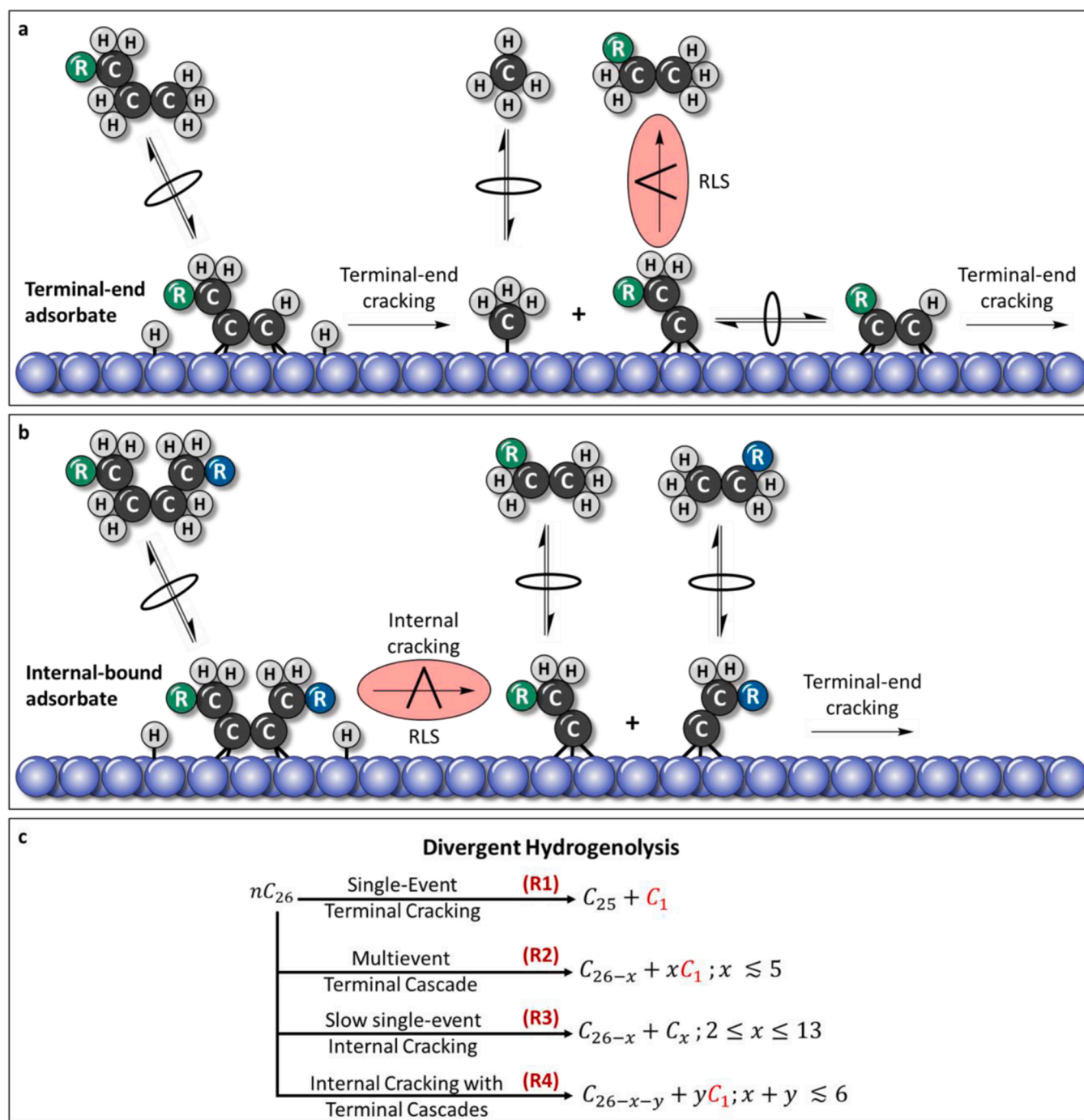


Fig. 5. Conceptual reaction network for large alkane hydrogenolysis over Ni/SiO₂. a, Cracking pathway for terminal-bound adsorbates. b, Cracking pathway for internally-bound adsorbates. c, Proposed divergent hydrogenolysis reaction network.

($M_w \sim 35$ kDa), and everyday materials, such as a PE bottle and PP bottle cap (Fig. 6a). The 76LDPE is 9x less reactive than the 4LDPE to achieve comparable solid yields (Fig. 6a) and has a 5 % higher selectivity towards methane (Fig. S30) indicating deeper R4 cascades. The decreased activity is likely due to the higher density of C-C bonds per polymer. This requires Ni to facilitate a higher number of turnovers before the molecular weight distribution in the solids residues is amenable to producing liquid (C₆-C₃₅) products. Virgin PPs are more reactive than 4LDPE, underscoring a polymer structure effect. Hydrogenolysis over Ni is known to be sensitive towards the structure of model alkanes. C-C terminal carbons are approximately tenfold more active than interior bonds [39]. PP has an abundance of terminal carbons

within the polymer chain equivalent to the number of monomer units, whereas 4LDPE is practically devoid of terminal carbons. We attribute the increased activity of PP substrates to the large presence of methyl groups along the chain which serve as initiation centers. Everyday materials are less reactive than virgin granules, but comparable yields are achieved with longer reaction times (12 h). The decreased activity is ascribed to effects from molecular weight, performance additives, or heteroatom impurities which have been identified to influence plastics deconstruction [16,23,57]. Additional studies are needed to understand the impact of additives and feedstock molecular weight on polyolefin hydrogenolysis. The liquid (C₆-C₃₅) product depends distinctly on the PO (Fig. S30). PP generates primarily iso-alkanes. The branched

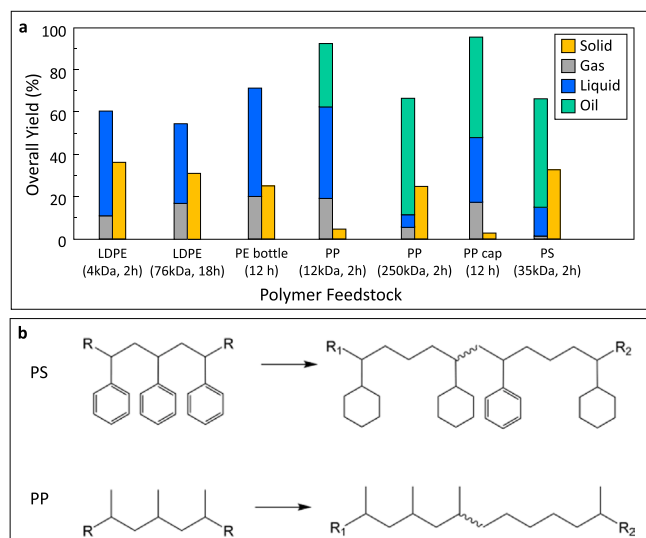


Fig. 6. Hydrogenolysis of virgin and commercial plastics over 15Ni/SiO₂. a, Solid, gas (C₁–C₅), liquid (C₆–C₃₅), and oil (C₁₀₀+) yields. b, Structural components in the PS and PP oils. Reaction conditions: 2.0 g polymer, 200 mg catalyst, 300 °C, 30 bar H₂ with reaction times noted for each polymer.

structure of C₂₀+ renders it ideal for lubricant base oils. PP also forms heavy liquid oils (C₁₀₀+) (GPC analysis, Table S2 and Fig. S31). The primary structural components, identified by liquid ¹³C NMR (Fig. 6b and Fig. S32), indicate that the PP oil retains the repeating PP units. (CH₂)_m segments are imparted on the chain from CH₃ cleavage, similar to Ru/TiO₂ [19].

15Ni/SiO₂ was also able to deconstruct virgin PS to heavy liquid oils (C₁₀₀+) and small liquid fragments (C₆–C₃₀) with negligible gas production. Liquid products are predominately cyclic alkanes (i.e., methylcyclohexane and ethylcyclohexane), small fractions of aromatics, and moderate fractions of hydrogenated dimers and trimers. The structure of the PS oil is distinct from the oil from PP (GPC analysis, Table S2 and Fig. S31). ¹³C and HSQC NMR show that the PS is hydrogenated to alicyclic cyclohexyl side-chains (Fig. 6b and Fig. S33–34) with new CH₂ groups emerging from C–C bond scission of the side-chains. Excitingly, these results demonstrate the hydrogenolysis chemistry can be expanded to PS polymers for oil production. Key goals for future PS deconstruction to base-oils via hydrogenolysis are to 1) maximize ring hydrogenation to enhance the oil stability and 2) target C–C scission to open the hydrogenated cyclohexyl rings.

4. Conclusions

We have discovered a simple Ni/SiO₂ catalyst with comparable performance to Ru- and better than Pt-based catalysts, expanding the viable catalysts to earth-abundant metals. Unexpectedly, hydrogenolysis proceeds via single and multiple cracking events mainly on internal polymer bonds and terminal liquid product bonds. This transition in pathways with molecular weight stems from the stronger adhesion of macromolecules, the much higher catalyst activity for terminal scissions, and the ratio of the terminal to internal bonds. One could engineer the strong metal-polymer binding via catalyst design (i.e., bimetallics, metal-support interactions, etc.) to dissuade successive reactions that lead to methane. The catalyst is applicable to multiple feedstocks, producing a structurally diverse and feedstock-dependent slate of products. This versatility combined with its low cost and abundance provide an essential step toward commercialization.

CRedit authorship contribution statement

Brandon C. Vance: Conceptualization, Methodology, Investigation,

Software, Validation, Formal analysis, Writing – original draft, Writing – review & editing. **Pavel A. Kots:** Conceptualization, Methodology, Investigation, Formal analysis, Writing – original draft, Writing – review & editing. **Cong Wang:** Formal analysis. **Jack E. Granite:** Investigation. **Dionisios G. Vlachos:** Conceptualization, Writing – review & editing, Project administration, Funding acquisition.

Declaration of Competing Interest

The authors declare the following financial interests/personal relationships which may be considered as potential competing interests: Dionisios Vlachos, Brandon Vance, Pavel Kots, and Cong Wang has patent #PCT/US2022/019667 pending to University of Delaware.

Data availability

Data will be made available on request.

Acknowledgements

This work was supported as part of the Center for Plastics Innovation, an Energy Frontier Research Center funded by the U.S. Department of Energy, Office of Science, Basic Energy Sciences under Grant Number DE-SC0021166. B.C.V. acknowledges a Graduate Research Fellowship through the National Science Foundation under Grant Number 1940700. This research used instruments in the Advanced Materials Characterization Lab (AMCL) at the University of Delaware. The authors used the NMR facilities at the University of Delaware, founded by the Delaware COBRE program, supported by a grant from the National Institute of General Medical Sciences – NIGMS (5 P30 GM110758-02) from the National Institutes of Health. Authors thank Dr. Shi Bai at the University of Delaware for his assistance with NMR measurements.

Appendix A. Supporting information

Supplementary data associated with this article can be found in the online version at doi:10.1016/j.apcatb.2022.122138.

References

- [1] R. Geyer, J.R. Jambeck, K.L. Law, Production, use, and fate of all plastics ever made, *Sci. Adv.* 3 (2017), e1700782, <https://doi.org/10.1126/sciadv.1700782>.
- [2] European Bioplastics, Nova-Institute, Bioplastics market development update 2020, Berlin, 2020. (<http://www.european-bioplastics.org/news/publications/>) (Accessed 1 December 2021).
- [3] US EPA - United States Environmental Protection Agency, Advancing sustainable materials management: 2017 Fact Sheet, United States Environ. Prot. Agency, Off. L. Emerg. Manag. Washington, DC 20460, (2019) 22, <https://doi.org/EPA530F-18-004>.
- [4] K.L. Law, N. Starr, T.R. Siegler, J.R. Jambeck, N.J. Mallos, G.H. Leonard, The United States' contribution of plastic waste to land and ocean, *Sci. Adv.* 6 (2020) eabd0288, <https://doi.org/10.1126/sciadv.abd0288>.
- [5] R. Lehner, C. Weder, A. Petri-Fink, B. Rothen-Rutishauser, Emergence of nanoplastic in the environment and possible impact on human health, *Environ. Sci. Technol.* 53 (2019) 1748–1765, <https://doi.org/10.1021/acs.est.8b05512>.
- [6] G.G.N. Thushari, J.D.M. Senevirathna, Plastic pollution in the marine environment, *Heliyon* 6 (2020), e04709, <https://doi.org/10.1016/j.heliyon.2020.e04709>.
- [7] M.C. Rillig, S.W. Kim, T.Y. Kim, W.R. Waldman, The global plastic toxicity debt, *Environ. Sci. Technol.* 55 (2021) 2717–2719, <https://doi.org/10.1021/acs.est.0c07781>.
- [8] Y. Liu, Y. Wang, N. Li, S. Jiang, Avobenzone and nanoplastics affect the development of zebrafish nervous system and retinal system and inhibit their locomotor behavior, *Sci. Total Environ.* 806 (2022), 150681, <https://doi.org/10.1016/j.scitotenv.2021.150681>.
- [9] J.C. Prata, J.P. da Costa, I. Lopes, A.C. Duarte, T. Rocha-Santos, Environmental exposure to microplastics: an overview on possible human health effects, *Sci. Total Environ.* 702 (2020), 134455, <https://doi.org/10.1016/J.SCITOTENV.2019.134455>.
- [10] A.R. Rahimi, J.M. García, Chemical recycling of waste plastics for new materials production, *Nat. Rev. Chem.* 1 (2017) 1–11, <https://doi.org/10.1038/s41570-017-0046>.
- [11] G. Celik, R.M. Kennedy, R.A. Hackler, M. Ferrandon, A. Tennakoon, S. Patnaik, A. M. Lapointe, S.C. Ammal, A. Heyden, F.A. Perras, M. Pruski, S.L. Scott, K. R. Poeppelmeier, A.D. Sadow, M. Delferro, Upcycling single-use polyethylene into

- high-quality liquid products, *ACS Cent. Sci.* 5 (2019) 1795–1803, <https://doi.org/10.1021/acscentsci.9b00722>.
- [12] A. Tennakoon, X. Wu, A.L. Paterson, S. Patnaik, Y. Pei, A.M. LaPointe, S.C. Ammal, R.A. Hackler, A. Heyden, I.I. Slowing, G.W. Coates, M. Delferro, B. Peters, W. Huang, A.D. Sadow, F.A. Perras, Catalytic upcycling of high-density polyethylene via a processive mechanism, *Nat. Catal.* 3 (2020) 893–901, <https://doi.org/10.1038/s41929-020-00519-4>.
 - [13] L. Chen, L.C. Meyer, L. Kovarik, D. Meira, X.I. Pereira-Hernandez, H. Shi, K. Khivantsev, O.Y. Gutiérrez, J. Szanyi, Disordered, sub-nanometer Ru structures on CeO₂ are highly efficient and selective catalysts in polymer upcycling by hydrogenolysis, *ACS Catal.* 12 (2022) 4618–4627, <https://doi.org/10.1021/acscatal.2c00684>.
 - [14] C. Jia, S. Xie, W. Zhang, N.N. Intan, J. Sampath, J. Pfandtner, H. Lin, Deconstruction of high-density polyethylene into liquid hydrocarbon fuels and lubricants by hydrogenolysis over Ru catalyst, *Chem. Catal.* 1 (2021) 437–455, <https://doi.org/10.1016/j.checat.2021.04.002>.
 - [15] J.E. Rorrer, G.T. Beckham, Y. Román-Leshkov, Conversion of polyolefin waste to liquid alkanes with Ru-based catalysts under mild conditions, *JACS Au* 1 (2021) 8–12, <https://doi.org/10.1021/jacsau.0c00041>.
 - [16] Y. Nakaji, M. Tamura, S. Miyaoka, S. Kumagai, M. Tanji, Y. Nakagawa, T. Yoshioka, K. Tomishige, Low-temperature catalytic upgrading of waste polyolefinic plastics into liquid fuels and waxes, *Appl. Catal. B Environ.* 285 (2021), 119805, <https://doi.org/10.1016/j.apcatb.2020.119805>.
 - [17] J.E. Rorrer, C. Troyano-Valls, G.T. Beckham, Y. Román-Leshkov, Hydrogenolysis of polypropylene and mixed polyolefin plastic waste over Ru/C to produce liquid alkanes, *ACS Sustain. Chem. Eng.* 9 (2021) 11661–11666, <https://doi.org/10.1021/acsschemeng.1c03786>.
 - [18] Y. Jing, Y. Wang, S. Furukawa, J. Xia, C. Sun, M.J. Hülsley, H. Wang, Y. Guo, X. Liu, N. Yan, Towards the circular economy: converting aromatic plastic waste back to arenes over a Ru/Nb₂O₅ catalyst, *Angew. Chem.* 133 (2021) 5587–5595, <https://doi.org/10.1002/ange.202011063>.
 - [19] P.A. Kots, S. Liu, B.C. Vance, C. Wang, J.D. Sheehan, D.G. Vlachos, Polypropylene plastic waste conversion to lubricants over Ru/TiO₂ catalysts, *ACS Catal.* 11 (2021) 8104–8115, <https://doi.org/10.1021/acscatal.1c00874>.
 - [20] C. Wang, T. Xie, P.A. Kots, B.C. Vance, K. Yu, P. Kumar, J. Fu, S. Liu, G. Tsilomelekis, E.A. Stach, W. Zheng, D.G. Vlachos, Polyethylene hydrogenolysis at mild conditions over ruthenium on tungstated zirconia, *JACS Au* 1 (2021) 1422–1434, <https://doi.org/10.1021/jacsau.1c00200>.
 - [21] S.D. Jaydev, A.J. Martín, J. Pérez-Ramírez, Direct conversion of polypropylene into liquid hydrocarbons on carbon-supported platinum catalysts, *ChemSusChem* 14 (2021) 1–8, <https://doi.org/10.1002/cssc.202101999>.
 - [22] L. Chen, Y. Zhu, L.C. Meyer, L.V. Hale, T.T. Le, A. Karkamkar, J.A. Lercher, O. Y. Gutiérrez, J. Szanyi, Effect of reaction conditions on the hydrogenolysis of polypropylene and polyethylene into gas and liquid alkanes, *React. Chem. Eng.* (2022), <https://doi.org/10.1039/D1RE00431J>.
 - [23] S. Liu, P.A. Kots, B.C. Vance, A. Danielson, D.G. Vlachos, Plastic waste to fuels by hydrocracking at mild conditions, *Sci. Adv.* 7 (2021) eabf8283, <https://doi.org/10.1126/SCIADV.ABF8283>.
 - [24] B.C. Vance, P.A. Kots, C. Wang, Z.R. Hinton, C.M. Quinn, T.H. Epps, L.S.T.J. Korley, D.G. Vlachos, Single pot catalyst strategy to branched products via adhesive isomerization and hydrocracking of polyethylene over platinum tungstated zirconia, *Appl. Catal. B Environ.* 299 (2021), 120483, <https://doi.org/10.1016/j.apcatb.2021.120483>.
 - [25] A. bin Jumah, A.A. Tedstone, A.A. Garforth, Hydrocracking of virgin and post-consumer polymers, *Microporous Mesoporous Mater.* 315 (2021), 110912, <https://doi.org/10.1016/j.micromeso.2021.110912>.
 - [26] T. Maqsood, J. Dai, Y. Zhang, M. Guang, B. Li, Pyrolysis of plastic species: a review of resources and products, *J. Anal. Appl. Pyrolysis* 159 (2021), 105295, <https://doi.org/10.1016/j.jaap.2021.105295>.
 - [27] M.M. Hasan, N. Batalha, G. Fraga, M.H.M. Ahmed, L. Pinard, M. Konarova, S. Pratt, B. Laycock, Zeolite shape selectivity impact on LDPE and PP catalytic pyrolysis products and coke nature, *Sustain. Energy Fuels* 6 (2022) 1587–1602, <https://doi.org/10.1039/D2SE00146B>.
 - [28] X. Jia, C. Qin, T. Friedberger, Z. Guan, Z. Huang, Efficient and selective degradation of polyethylenes into liquid fuels and waxes under mild conditions, *Sci. Adv.* 2 (2016), e1501591, <https://doi.org/10.1126/sciadv.1501591>.
 - [29] L.D. Ellis, S.V. Orski, G.A. Kenlaw, A.G. Norman, K.L. Beers, Y. Román-Leshkov, G. T. Beckham, Tandem heterogeneous catalysis for polyethylene depolymerization via an olefin-intermediate process, *ACS Sustain. Chem. Eng.* 9 (2021) 623–628, <https://doi.org/10.1021/ACSSUSCHEMENG.0C07612/ASSET/IMAGES/LARGE/SC0C07612.0002.JPEG>.
 - [30] L. Yao, J. King, D. Wu, S.S.C. Chuang, Z. Peng, Non-thermal plasma-assisted hydrogenolysis of polyethylene to light hydrocarbons, *Catal. Commun.* 150 (2021), 106274, <https://doi.org/10.1016/j.cattcom.2020.106274>.
 - [31] N. Zhou, L. Dai, Y. Lyu, H. Li, W. Deng, F. Guo, P. Chen, H. Lei, R. Ruan, Catalytic pyrolysis of plastic wastes in a continuous microwave assisted pyrolysis system for fuel production, *Chem. Eng. J.* 418 (2021), 129412, <https://doi.org/10.1016/j.cej.2021.129412>.
 - [32] U.S. Geological Survey, Mineral Commodity Summaries 2021, 2021. <https://doi.org/https://doi.org/10.3133/mcs2021>.
 - [33] U.S. Geological Survey, Metal Prices in the United States Through 2010, 2012. <http://www.usgs.gov/pubprod> (Accessed 1 December 2021).
 - [34] R.M. Bullock, J.G. Che, L. Gagliardi, P.J. Chiri, O.K. Farh, C.H. Hendo, C.W. Jone, J.A. Keit, J. Klosin, S.D. Mintee, R.H. Morri, A.T. Radosevic, T.B. Rauchfus, N. A. Strotma, A. Vojvodic, T.R. War, J.Y. Yan, Y. Surendranath, Using nature's blueprint to expand catalysis with Earth-abundant metals, *Science* 369 (2020), https://doi.org/10.1126/SCIENCE.ABC3183/ASSET/34F333DE-9183-4D3C-ADD1-7AAAAB8FF1E4/ASSETS/GRAPHIC/369_ABC3183_F6.JPEG.
 - [35] P.R. Robinson, G.E. Dolbear, Hydrotreating and hydrocracking: fundamentals, *Pract. Adv. Pet. Process* (2007) 177–218, https://doi.org/10.1007/978-0-387-25789-1_7.
 - [36] H. Matsumoto, Y. Saito, Y. Yoneda, The classification of metal catalysts in hydrogenolysis of hexane isomers, *J. Catal.* 22 (1971) 182–192, [https://doi.org/10.1016/0021-9517\(71\)90184-9](https://doi.org/10.1016/0021-9517(71)90184-9).
 - [37] J.H. Sinfelt, Specificity in catalytic hydrogenolysis by metals, *Adv. Catal.* 23 (1973) 91–119, [https://doi.org/10.1016/S0360-0564\(08\)60299-0](https://doi.org/10.1016/S0360-0564(08)60299-0).
 - [38] C.J. Machiels, R.B. Anderson, Hydrogenolysis of 2,3-dimethylbutane on supported ruthenium, nickel, cobalt, and iron, *J. Catal.* 58 (1979) 260–267, [https://doi.org/10.1016/0021-9517\(79\)90263-X](https://doi.org/10.1016/0021-9517(79)90263-X).
 - [39] G. Leclercq, S. Pietrzyk, M. Peyroux, M. Karroua, Hydrogenolysis of saturated hydrocarbons. V. Influence of hydrocarbon structures on the activity and selectivity of Ni on silica, *J. Catal.* 99 (1986) 1–11, [https://doi.org/10.1016/0021-9517\(86\)90192-2](https://doi.org/10.1016/0021-9517(86)90192-2).
 - [40] J.H. Miller, A.K. Starace, D.A. Ruddy, Catalytic activation of polyethylene model compounds over metal-exchanged beta zeolites, *ChemSusChem* 15 (2022), e202200535, <https://doi.org/10.1002/cssc.202200535>.
 - [41] J.M. Escola, D.P. Serrano, J. Aguado, L. Briones, Hydroreforming of the LDPE thermal cracking oil over hierarchical Ni/beta catalysts with different Ni particle size distributions, *Ind. Eng. Chem. Res.* 54 (2015) 6660–6668, https://doi.org/10.1021/ACS.IECR.5B01160/ASSET/IMAGES/LARGE/IE-2015-01160U_0009.JPEG.
 - [42] J.M. Escola, D.P. Serrano, M. Arroyo, A. Alba, Conversion of LDPE into transportation fuels by a two-stage process using Ni/Al-SBA-15 as catalyst, *J. Mater. Cycles Waste Manag.* 16 (2014) 435–441, <https://doi.org/10.1007/S10163-014-0249-7/TABLES/2>.
 - [43] J.M. Escola, J. Aguado, D.P. Serrano, L. Briones, Hydroreforming over Ni/H-beta of the thermal cracking products of LDPE, HDPE and PP for fuel production, *J. Mater. Cycles Waste Manag.* 14 (2012) 286–293, <https://doi.org/10.1007/S10163-012-0054-0/TABLES/3>.
 - [44] S. Tada, M. Yokoyama, R. Kikuchi, T. Haneda, H. Kameyama, N₂O pulse titration of Ni/α-Al₂O₃ catalysts: a new technique applicable to nickel surface-area determination of nickel-based, *Catal., J. Phys. Chem. C* 117 (2013) 14652–14658, <https://doi.org/10.1021/JP404291K>.
 - [45] D.T. Gillespie, Exact stochastic simulation of coupled chemical reactions with delays, *J. Chem. Phys. Chem.* 81 (1977) 2340–2361, <https://doi.org/10.1063/1.2710253>.
 - [46] S.L. Tait, Z. Dohnálek, C.T. Campbell, B.D. Kay, n-alkanes on Pt(111) and on C (0001)/Pt(111): chain length dependence of kinetic desorption parameters, *J. Chem. Phys.* 125 (2006), 234308, <https://doi.org/10.1063/1.2400235>.
 - [47] K.R. Paserba, A.J. Gellman, Effects of conformational isomerism on the desorption kinetics of n-alkanes from graphite, *J. Chem. Phys.* 115 (2001) 6737, <https://doi.org/10.1063/1.1398574>.
 - [48] K. Kochloeff, V. Bázant, Hydrogenolysis of saturated hydrocarbons on a nickel catalyst. I. Kinetics of hydrogenolysis of ethylcyclohexane and reactivity of alkylcyclohexanes, *J. Catal.* 8 (1967) 250–260, [https://doi.org/10.1016/0021-9517\(67\)90312-0](https://doi.org/10.1016/0021-9517(67)90312-0).
 - [49] B. Coq, A. Bittar, F. Figueras, Hydrogenolysis and isomerization of alkanes on Ru/AlO₃ catalysts of varying dispersions, *Appl. Catal.* 59 (1990) 103–121, [https://doi.org/10.1016/S0166-9834\(00\)82190-9](https://doi.org/10.1016/S0166-9834(00)82190-9).
 - [50] L.D. Schmidt, K.R. Krause, Correlation between microstructure and hydrogenolysis activity and selectivity of noble metal catalyst particles, *Catal. Today* 12 (1992) 269–282, [https://doi.org/10.1016/0920-5861\(92\)85045-N](https://doi.org/10.1016/0920-5861(92)85045-N).
 - [51] D.W. Flaherty, D.D. Hibbitts, E. Iglesia, Metal-catalyzed C–C bond cleavage in alkanes: effects of methyl substitution on transition-state structures and stability, *J. Am. Chem. Soc.* 136 (2014) 9664–9676, <https://doi.org/10.1021/ja5037429>.
 - [52] G.B. Galland, R.F. De Souza, R.S. Mauler, F.F. Nunes, ¹³C NMR determination of the composition of linear low-density polyethylene obtained with [η3-methallyl-nickel-diimine]PF₆ complex, *Macromolecules* 32 (1999) 1620–1625, <https://doi.org/10.1021/MA981669H/ASSET/IMAGES/MEDIUM/MA981669HE00050.GIF>.
 - [53] X. Peng, C. Cheng, J. Kang, B. Gu, X. Yu, Q. Zhang, Y. Wang, Impact of hydrogenolysis on the selectivity of the fischer–tropsh synthesis: diesel fuel production over mesoporous zeolite-Y-supported cobalt nanoparticles, *Angew. Chem. Int. Ed.* 54 (2015) 4553–4556, <https://doi.org/10.1002/ANIE.201411708>.
 - [54] E. Kikuchi, Y. Morita, Hydrogenolysis of n-pentane on nickel catalyst, *J. Catal.* 15 (1969) 217–223, [https://doi.org/10.1016/0021-9517\(69\)90283-8](https://doi.org/10.1016/0021-9517(69)90283-8).
 - [55] P.A. Kots, B.C. Vance, D.G. Vlachos, Polyolefin plastic waste hydroconversion to fuels, lubricants, and waxes: a comparative study, *React. Chem. Eng.* 7 (2022) 41–54, <https://doi.org/10.1039/d1re00447f>.
 - [56] Y. Nakagawa, S.I. Oya, D. Kanno, Y. Nakaji, M. Tamura, K. Tomishige, Regioselectivity and reaction mechanism of Ru-catalyzed hydrogenolysis of squalane and model alkanes, *ChemSusChem* 10 (2017) 189–198, <https://doi.org/10.1002/cssc.201601204>.
 - [57] Z.R. Hinton, P.A. Kots, M. Soukaseum, B.C. Vance, D.G. Vlachos, T.H. Epps, L.S.T. J. Korley, Antioxidant-induced transformations of a metal-acid hydrocracking catalyst in the deconstruction of polyethylene waste, *Green Chem.* (2022), <https://doi.org/10.1039/d2gc02503e>.